

Harmonic Power-Flow Study of Polyphase Grids with Converter-Interfaced Distributed Energy Resources, Part II: Model Library and Validation

Johanna Kristin Maria Becker, *Member, IEEE*, Andreas Martin Kettner, *Member, IEEE*, Lorenzo Reyes-Chamorro, *Senior Member, IEEE*, Zhixiang Zou, *Member, IEEE*, Marco Liserre, *Fellow, IEEE*, and Mario Paolone, *Senior Member, IEEE*

Abstract—In Part I, a method for the *Harmonic Power-Flow* (HPF) study of three-phase power grids with *Converter-Interfaced Distributed Energy Resources* (CIDERs) is proposed. The method is based on generic and modular representations of the grid and the CIDERs, and explicitly accounts for coupling between harmonics. In Part II, the HPF method is validated. First, the applicability of the modeling framework is demonstrated on typical grid-forming and grid-following CIDERs. Then, the HPF method is implemented in Matlab and compared against time-domain simulations with Simulink. The accuracy of the models and the performance of the solution algorithm are assessed for individual resources and a modified version of the CIGRÉ low-voltage benchmark microgrid (i.e., with additional unbalanced components). The observed maximum errors are 6.3E-5 p.u. w.r.t. voltage magnitude, 1.3E-3 p.u. w.r.t. current magnitude, and 0.9 deg w.r.t. phase. Moreover, the scalability of the method is assessed w.r.t. the number of CIDERs and the maximum harmonic order (≤ 25). For the maximum problem size, the execution time of the HPF method is 6.52 sec, which is 5 times faster than the time-domain simulation. The convergence of the method is robust w.r.t. the choice of the initial point, and multiplicity of solutions has not been observed.

Index Terms—Distributed energy resources, harmonic power-flow study, polyphase power systems, power electronic converters, unbalanced power grids.

NOMENCLATURE

Component Models	
π	The power hardware of a CIDER
κ	The control software of a CIDER
α	The actuator of a CIDER
λ	A stage in the cascaded structure of a CIDER ($\lambda \in \{1, \dots, \Lambda\}$)

J. Becker, and M. Paolone are with the Distributed Electrical Systems Laboratory at the École Polytechnique Fédérale de Lausanne (EPFL) in CH-1015 Lausanne, Switzerland (E-mail: {johanna.becker, mario.paolone}@epfl.ch).

A. Kettner is with PSI NEPLAN AG, 8700 Küsnacht, Switzerland (E-mail: andreas.kettner@neplan.ch).

L. Reyes-Chamorro is with the Facultad de Ciencias de la Ingeniería at the Universidad Austral de Chile (UACH) in CL-5111187 Valdivia, Chile (E-mail: lorenzo.reyes@uach.cl).

Z. Zou is with the School of Electrical Engineering, Southeast University, in PRC-210096 Nanjing, China (E-mail: zzou@seu.edu.cn).

M. Liserre is with the Chair of Power Electronics at the Christian-Albrechts-Universität zu Kiel (CAU) in DE-24143 Kiel, Germany (E-mail: ml@tf.uni-kiel.de).

This work was funded by the Schweizerischer Nationalfonds (SNF, Swiss National Science Foundation) via the National Research Programme NRP 70 “Energy Turnaround” (NRP 70 “Energy Turnaround” (projects nr. 173661 and 197060) and by the Deutsche Forschungsgemeinschaft (DFG, German Research Foundation) via the Priority Programme DFG SPP 1984 “Hybrid and Multimodal Energy Systems” (project nr. 359982322).

v_λ	The voltage in a capacitive filter stage λ
i_λ	The current in an inductive filter stage λ
R_λ, L_λ	The compound electrical parameters of an inductive filter stage λ
G_λ, C_λ	The compound electrical parameters of a capacitive filter stage λ
$K_{FB,\lambda}$	The feed-back gain of a controller stage λ
$T_{FB,\lambda}$	The integration time of a controller stage λ
$K_{FF,\lambda}$	The feed-forward gain of a controller stage λ
$K_{FT,\lambda}$	The feed-through gain of a controller stage λ

Resource Models

γ	The power grid
ρ	The reference calculation of a CIDER
σ	The setpoint of a CIDER
f_1	The fundamental frequency ($f_1 := \frac{1}{T}$)
$h \in \mathcal{H}$	A harmonic order ($\mathcal{H} := \{-h_{\max}, \dots, h_{\max}\}$)
θ	A given reference angle
$\tau_{\kappa \pi}$	A change of reference frame from π to κ
$\mathbf{T}_{\kappa \pi}(t)$	The LTP matrix which describes $\tau_{\kappa \pi}$
$\mathbf{T}_{\kappa \pi,h}$	The Fourier coefficient of $\mathbf{T}_{\pi \gamma}$ ($h \in \mathcal{H}$)
$\hat{\mathbf{T}}_{\kappa \pi}$	The Toeplitz matrix composed of the $\hat{\mathbf{T}}_{\kappa \pi,h}$
$\mathbf{x}(t)$	The state vector of a state-space model
$\mathbf{u}(t)$	The input vector of a state-space model
$\mathbf{y}(t)$	The output vector of a state-space model
$\mathbf{w}(t)$	The disturbance vector of a state-space model
$\mathbf{A}(t)$	The system matrix of an LTP system
$\mathbf{B}(t)$	The input matrix of an LTP system
$\mathbf{C}(t)$	The output matrix of an LTP system
$\mathbf{D}(t)$	The feed-through matrix of an LTP system
$\mathbf{E}(t)$	The input disturbance matrix of an LTP system
$\mathbf{F}(t)$	The output disturbance matrix of an LTP system
V_σ	The voltage setpoint of a grid-forming resource
S_σ	The power setpoint of a grid-following resource
$v_{\gamma,D}(t)$	The direct component of v_γ
$v_{\gamma,Q}(t)$	The quadrature component of v_γ
$\xi_D(t)$	The time-variant signal content of $v_{\gamma,D}(t)$
$V_{\gamma,D,h}$	The Fourier coefficient of $v_{\gamma,D}(t)$ ($h \in \mathcal{H}$)

Validation

\mathbf{X}_h	The Fourier coefficient of a polyphase electrical quantity ($h \in \mathcal{H}$)
$e_{\text{abs}}(\mathbf{X}_h)$	The maximum absolute error over all phases w.r.t. $ \mathbf{X}_h $ between HPF and TDS

$e_{\arg}(\mathbf{X}_h)$	The maximum absolute error over all phases w.r.t. $\angle \mathbf{X}_h$ between HPF and TDS
$(\cdot)_{+/-/0}$	Positive-, negative-, and homopolar-sequence components of a three-phase electrical quantity.
$T_{exc,HPF}$	The execution time of the HPF
$\mu(\cdot)$	The mean value operator
$\sigma(\cdot)$	The standard deviation operator

I. INTRODUCTION

THE validation of the proposed *Harmonic Power-Flow* (HPF) method involves two aspects. Firstly, the suitability of the modeling framework to represent common types of *Converter-Interfaced Distributed Energy Resources* (CIDERs) with grid-forming or grid-following controls has to be confirmed. In this respect, power converters equipped with either LC or LCL filters are considered. Secondly, the accuracy of the modeling framework and the performance of the solution algorithm need to be assessed. To this end, the proposed method is applied to analyze individual resources as well as an entire system. More precisely, the HPF algorithm is implemented in Matlab and compared against time-domain simulations carried out in Simulink.

The remainder of Part II is organized as follows: First, the models of standard components of CIDERs (i.e., actuator, filters, and controllers) are developed in Section II, including a thorough discussion of their properties and working principles. These component models are combined in Section III to construct the complete models of a grid-forming and a grid-following CIDER. Then, the proposed method is tested on individual resources in Section IV, as well as on the CIGRÉ low-voltage benchmark microgrid in Section V. Finally, the conclusions are drawn in Section VI.

II. LIBRARY OF COMPONENT MODELS

In this section, the models of actuators, filters, and controllers are developed. Note that, in order to obtain compact formulas, the time-dependency of the electrical quantities and signals is not explicitly stated each time.

A. Actuator

The actuator is the power converter which interfaces the DC side of the CIDER (i.e., a source or load) with its AC side (i.e., the filter). It consists of an array of switches (i.e., power-transistor-type devices), which are controlled so that the output voltage of the actuator \mathbf{v}_α follows the reference $\mathbf{v}_{\alpha,\pi}^*$ (see Fig. 1). The switching signals are typically generated by a *Pulse-Width Modulator* (PWM). This modulation creates distortions in the output voltage of the power converter. Indeed, this is why a filter is needed. Typically, these distortions occur at high frequencies (i.e., several kHz), which are far beyond the frequency range that is of interest for harmonic analysis (i.e., up to 1-2 kHz) [1]. Hence, the actuator can be regarded as ideal voltage source in the HPF study:

Hypothesis 1. *In the frequency range of interest for the HPF study, switching effects are negligible. Therefore, the actuator is regarded as ideal voltage source:*

$$\mathbf{v}_{\alpha,\pi} = \mathbf{v}_{\alpha,\pi}^* \in \mathbb{R}^{\dim(\pi) \times 1} \quad (1)$$

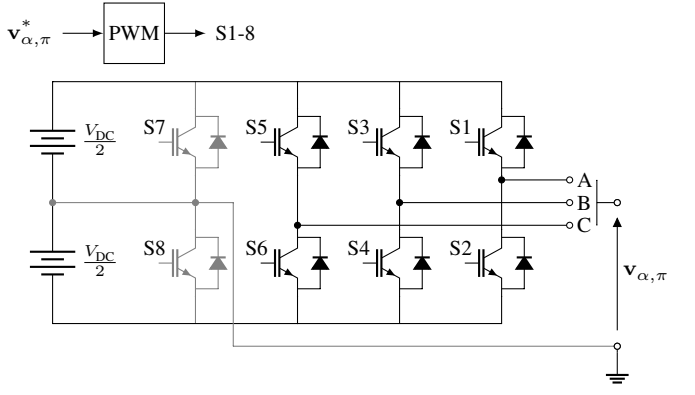


Fig. 1. Schematic diagram of a three-phase two-level power converter, which is commonly used for CIDERs. The fourth leg is optional: it is required only if the power converter has to be able to inject or absorb homopolar currents.

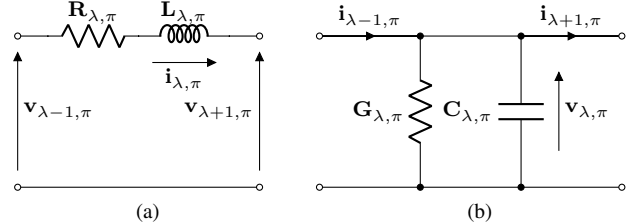


Fig. 2. Equivalent circuits of a filter stage λ constructed from inductors (2a) or capacitors (2b), respectively. Observe that voltages, currents, and electrical parameters are expressed in the reference frame of the power hardware π .

Note that the size of this vector depends on the reference frame in which the power hardware is modelled¹.

B. Filter Stages

In order to attenuate the high-frequency distortions resulting from the switching in the actuator, CIDERs are equipped with cascades of filter stages [2]. Each stage consists of inductors or capacitors, which filter currents or voltages, respectively. Notably, the commonly used L-, LC-, and LCL-filters as well as higher-order filters are built in this way.

Consider any stage λ in the cascade of filters. An inductive filter stage is represented by the equivalent circuit in Fig. 2a, which is described by the following differential equation:

$$\mathbf{v}_{\lambda-1,\pi} - \mathbf{v}_{\lambda+1,\pi} = \mathbf{R}_{\lambda,\pi} \mathbf{i}_{\lambda,\pi} + \mathbf{L}_{\lambda,\pi} \frac{d}{dt} \mathbf{i}_{\lambda,\pi} \quad (2)$$

$\mathbf{R}_{\lambda,\pi}, \mathbf{L}_{\lambda,\pi} \in \mathbb{R}^{\dim(\pi) \times \dim(\pi)}$ are the compound electrical parameters of the inductive filter stage, $\mathbf{i}_{\lambda,\pi} \in \mathbb{R}^{\dim(\pi) \times 1}$ is the current flowing through it, and $\mathbf{v}_{\lambda-1,\pi}, \mathbf{v}_{\lambda+1,\pi} \in \mathbb{R}^{\dim(\pi) \times 1}$ are the voltages at the start and end node of the stage, respectively. Again, the sizes of these vectors and matrices depend on the reference frame in which the power hardware is modelled. A capacitive filter stage is represented by the equivalent circuit in Fig. 2b, which is described by

$$\mathbf{i}_{\lambda-1,\pi} - \mathbf{i}_{\lambda+1,\pi} = \mathbf{G}_{\lambda,\pi} \mathbf{v}_{\lambda,\pi} + \mathbf{C}_{\lambda,\pi} \frac{d}{dt} \mathbf{v}_{\lambda,\pi} \quad (3)$$

¹If phase coordinates are used, $\mathbf{v}_{\alpha,\pi}, \mathbf{v}_{\alpha,\pi}^* \in \mathbb{R}^{3 \times 1}$.

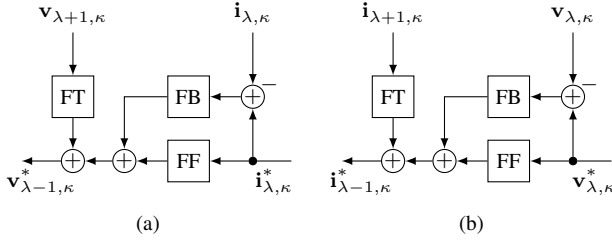


Fig. 3. Block diagrams of a controller stage λ associated with an inductive (3a) and capacitive (3b) filter stage, respectively. In general, the control law includes *Feed-Back* (FB), *Feed-Forward* (FF), and *Feed-Through* (FT) terms. Observe that voltages and currents are expressed in the reference frame of the control software κ .

$\mathbf{G}_{\lambda,\pi}, \mathbf{C}_{\lambda,\pi} \in \mathbb{R}^{\dim(\pi) \times \dim(\pi)}$ are the compound electrical parameters of the capacitive filter stage, $\mathbf{v}_{\lambda,\pi} \in \mathbb{R}^{\dim(\pi) \times 1}$ is the voltage across it, and $\mathbf{i}_{\lambda-1,\pi}, \mathbf{i}_{\lambda+1,\pi} \in \mathbb{R}^{\dim(\pi) \times 1}$ are the currents flowing into and out of the stage, respectively.

In practice, the filter stages are built from identical discrete elements (i.e., one element per phase). Accordingly, the following hypothesis can be made:

Hypothesis 2. *The compound electrical parameters of the filter stages are diagonal matrices with equal nonzero entries. That is, an inductive filter stage is characterized by*

$$\mathbf{R}_{\lambda,\pi} = R_\lambda \text{diag}(\mathbf{1}_\pi), \quad \mathbf{L}_{\lambda,\pi} = L_\lambda \text{diag}(\mathbf{1}_\pi) \quad (4)$$

and a capacitive filter stage by

$$\mathbf{G}_{\lambda,\pi} = G_\lambda \text{diag}(\mathbf{1}_\pi), \quad \mathbf{C}_{\lambda,\pi} = C_\lambda \text{diag}(\mathbf{1}_\pi) \quad (5)$$

where $\text{diag}(\mathbf{1}_\pi)$ is the identity matrix w.r.t. reference frame of the power hardware. R_λ, L_λ and G_λ, C_λ are the parameters of the discrete elements.

C. Controller Stages

Each filer stage can be coupled with a corresponding controller, which regulates either the current through or the voltage across the filter element, depending on whether the filter stage is inductive or capacitive.² As illustrated in Fig. 3, such a controller generally performs *Feed-Back* (FB), *Feed-Forward* (FF), and *Feed-Through* (FT) control. More precisely, as shown in Figs. 3a and 3b, a stage λ of the controller calculates the reference for the next-inner stage $\lambda - 1$ from the deviation between its own state and the desired reference (i.e., via FB and FF control), as well as the state of the next-outer stage $\lambda + 1$ (i.e., via FT control). In principle, each block of a controller stage could be composed of multiple subblocks connected in series or in parallel (e.g., for the mitigation of specific harmonics). In practice, simple *Proportional-Integral-Derivative* (PID) and *Proportional-Resonant* (PR) controllers are commonly used [3].

For the sake of illustration, PI-controllers are considered for FB control, and P-controllers for FF and FT control:

²As already mentioned in Part I of this paper, it is common practice for CIDERs with LCL filter to implement one instead of two current control loops. Notably, this can easily be represented in the proposed framework.

Hypothesis 3. *Each controller stage consists of a PI controller for FB control, and two P controllers for FF and FT controls.*

Let $\mathbf{K}_{\text{FB},\lambda}, \mathbf{K}_{\text{FF},\lambda}, \mathbf{K}_{\text{FT},\lambda} \in \mathbb{R}^{\dim(\kappa) \times \dim(\kappa)}$ be the proportional gains and $T_{\text{FB},\lambda}$ the integration time, respectively. The control law for an inductive filter stage is given by (see Fig. 3a)

$$\mathbf{v}_{\lambda-1,\kappa}^* = \begin{bmatrix} \mathbf{K}_{\text{FB},\lambda} \left(\Delta \mathbf{i}_{\lambda,\kappa} + \frac{1}{T_{\text{FB},\lambda}} \int \Delta \mathbf{i}_{\lambda,\kappa} dt \right) \\ + \mathbf{K}_{\text{FT},\lambda} \mathbf{v}_{\lambda+1,\kappa} + \mathbf{K}_{\text{FF},\lambda} \mathbf{i}_{\lambda,\kappa}^* \end{bmatrix} \quad (6)$$

$$\Delta \mathbf{i}_{\lambda,\kappa} := \mathbf{i}_{\lambda,\kappa}^* - \mathbf{i}_{\lambda,\kappa} \quad (7)$$

$\mathbf{v}_{\lambda-1,\kappa}^*, \mathbf{i}_{\lambda,\kappa}^* \in \mathbb{R}^{\dim(\kappa) \times 1}$ are the reference voltage at the input of the controller stage and the reference current at its output, respectively. $\mathbf{v}_{\lambda+1,\kappa}, \mathbf{i}_{\lambda,\kappa} \in \mathbb{R}^{\dim(\kappa) \times 1}$ are the voltage at the output of the filter stage and the current through it, respectively, expressed in the reference frame of the controller. The control law for a capacitive filter stage is analogous (see Fig. 3b):

$$\mathbf{i}_{\lambda-1,\kappa}^* = \begin{bmatrix} \mathbf{K}_{\text{FB},\lambda} \left(\Delta \mathbf{v}_{\lambda,\kappa} + \frac{1}{T_{\text{FB},\lambda}} \int \Delta \mathbf{v}_{\lambda,\kappa} dt \right) \\ + \mathbf{K}_{\text{FT},\lambda} \mathbf{i}_{\lambda+1,\kappa} + \mathbf{K}_{\text{FF},\lambda} \mathbf{v}_{\lambda,\kappa}^* \end{bmatrix} \quad (8)$$

$$\Delta \mathbf{v}_{\lambda,\kappa} := \mathbf{v}_{\lambda,\kappa}^* - \mathbf{v}_{\lambda,\kappa} \quad (9)$$

$\mathbf{i}_{\lambda-1,\kappa}^*, \mathbf{v}_{\lambda,\kappa}^* \in \mathbb{R}^{\dim(\kappa) \times 1}$ are the reference current at the input of the controller stage and the reference voltage at its output, respectively. $\mathbf{i}_{\lambda+1,\kappa}, \mathbf{v}_{\lambda,\kappa} \in \mathbb{R}^{\dim(\kappa) \times 1}$ are the current at the output of the filter stage and voltage across it, respectively, expressed in the reference frame of the controller.

Typically, the FB and FT controllers treat each coordinate in the reference frame separately, and apply equal gains to them. In line with this fact, the following hypothesis is made:

Hypothesis 4. *The FB and FT gains are diagonal matrices with equal nonzero entries. That is*

$$\mathbf{K}_{\text{FB},\lambda} = K_{\text{FB},\lambda} \text{diag}(\mathbf{1}_\kappa) \quad (10)$$

$$\mathbf{K}_{\text{FT},\lambda} = K_{\text{FT},\lambda} \text{diag}(\mathbf{1}_\kappa) \quad (11)$$

where $\text{diag}(\mathbf{1}_\kappa)$ is the identity matrix w.r.t. the reference frame of the controls software.

The FF controllers, by contrast, are obtained by restating the dynamical models of the filter stages, which are given in the reference frame of the power hardware, in the reference frame of the control software [4]. To this end, the transformation matrices $\mathbf{T}_{\kappa|\pi} \in \mathbb{R}^{\dim(\kappa) \times \dim(\pi)}$ and $\mathbf{T}_{\pi|\kappa} \in \mathbb{R}^{\dim(\pi) \times \dim(\kappa)}$ are substituted into the filter equations (2)–(3). For the inductive filter stage, one obtains

$$\mathbf{v}_{\lambda-1,\kappa} - \mathbf{v}_{\lambda+1,\kappa} = \mathbf{R}_{\lambda,\kappa} \mathbf{i}_{\lambda,\kappa} + \mathbf{L}_{\lambda,\kappa} \frac{d}{dt} \mathbf{i}_{\lambda,\kappa} \quad (12)$$

where $\mathbf{R}_{\lambda,\kappa}, \mathbf{L}_{\lambda,\kappa} \in \mathbb{R}^{\dim(\kappa) \times \dim(\kappa)}$ are given by

$$\mathbf{R}_{\lambda,\kappa} = \mathbf{T}_{\kappa|\pi} \mathbf{R}_{\lambda,\pi} \mathbf{T}_{\pi|\kappa} + \mathbf{T}_{\kappa|\pi} \mathbf{L}_{\lambda,\pi} \frac{d}{dt} \mathbf{T}_{\pi|\kappa} \quad (13)$$

$$\mathbf{L}_{\lambda,\kappa} = \mathbf{T}_{\kappa|\pi} \mathbf{L}_{\lambda,\pi} \mathbf{T}_{\pi|\kappa} \quad (14)$$

Analogously, for the capacitive filter stage, one finds

$$\mathbf{i}_{\lambda-1,\kappa} - \mathbf{i}_{\lambda+1,\kappa} = \mathbf{G}_{\lambda,\kappa} \mathbf{v}_{\lambda,\kappa} + \mathbf{C}_{\lambda,\kappa} \frac{d}{dt} \mathbf{v}_{\lambda,\kappa} \quad (15)$$

where $\mathbf{G}_{\lambda,\kappa}, \mathbf{C}_{\lambda,\kappa} \in \mathbb{R}^{\text{dim}(\kappa) \times \text{dim}(\kappa)}$ are given by

$$\mathbf{G}_{\lambda,\kappa} = \mathbf{T}_{\kappa|\pi} \mathbf{G}_{\lambda,\pi} \mathbf{T}_{\pi|\kappa} + \mathbf{T}_{\kappa|\pi} \mathbf{C}_{\lambda,\pi} \frac{d}{dt} \mathbf{T}_{\pi|\kappa} \quad (16)$$

$$\mathbf{C}_{\lambda,\kappa} = \mathbf{T}_{\kappa|\pi} \mathbf{C}_{\lambda,\pi} \mathbf{T}_{\pi|\kappa} \quad (17)$$

Observe that the expressions for $\mathbf{R}_{\lambda,\kappa}$ and $\mathbf{G}_{\lambda,\kappa}$ include terms which result from the temporal derivatives of $\mathbf{i}_{\lambda,\pi} = \mathbf{T}_{\pi|\kappa} \mathbf{i}_{\lambda,\kappa}$ and $\mathbf{v}_{\lambda,\pi} = \mathbf{T}_{\pi|\kappa} \mathbf{v}_{\lambda,\kappa}$, respectively. These expressions often turn out to be time-invariant thanks to Hyp. 2. For instance, as will be shown shortly, this is the case in the DQ frame.

Using (12) and (15), the FF gains can be set in order to achieve zero error in steady-state (e.g., [4]) via the following additional hypothesis.

Hypothesis 5. The FF gains are set to

$$\mathbf{K}_{\text{FF},\lambda} = \begin{cases} \mathbf{R}_{\lambda,\kappa} & \text{for inductive filter stages} \\ \mathbf{G}_{\lambda,\kappa} & \text{for capacitive filter stages} \end{cases} \quad (18)$$

III. LIBRARY OF RESOURCE MODELS

In this section, the models of typical grid-forming and grid-following CIDERS are constructed from the components presented in Section II, based on the generic LTP models defined in Part I.

A. Circuit Configurations and Reference Frames

Usually, the grid and the power hardware are both modeled in phase coordinates, but their circuit configuration may not be the same. The grid is a four-wire system (i.e., three phase plus one neutral conductor), whereas the power converters can be either four-leg or three-leg devices (i.e., with or without neutral conductor). If a CIDER with a four-leg power converter is connected to a four-wire grid, all sequence components (i.e., positive, negative, and homopolar sequences) of voltage and current can pass in both directions. This corresponds to

$$\mathbf{T}_{\pi|\gamma} = \mathbf{T}_{\gamma|\pi} = \text{diag}(\mathbf{1}_3) \quad (19)$$

By contrast, if a CIDER with a three-leg power converter is connected to a four-wire grid, homopolar sequences are blocked in both directions. This is represented by

$$\mathbf{T}_{\pi|\gamma} = \mathbf{T}_{\gamma|\pi} = \text{diag}(\mathbf{1}_3) - \frac{1}{3} \mathbf{1}_{3 \times 3} \quad (20)$$

It is common practice to implement the control software in *Direct-Quadrature* (DQ) components [3]. If the power hardware is modeled in phase (ABC) coordinates, as previously mentioned, one obtains

$$\mathbf{T}_{\kappa|\pi} = \mathbf{T}_{\pi|\kappa}^T \quad (21)$$

$$\mathbf{T}_{\pi|\kappa} = \sqrt{\frac{2}{3}} \begin{bmatrix} \cos(\theta) & -\sin(\theta) \\ \cos(\theta - \frac{2\pi}{3}) & -\sin(\theta - \frac{2\pi}{3}) \\ \cos(\theta + \frac{2\pi}{3}) & -\sin(\theta + \frac{2\pi}{3}) \end{bmatrix} \quad (22)$$

where θ is a given reference angle. How the reference angle is obtained, depends on the type of CIDER. Namely, it is calculated from a reference clock in grid-forming CIDERS, whereas a synchronisation unit is needed for grid-following CIDERS. In either case, it is assumed that θ is synchronized with the fundamental tone:

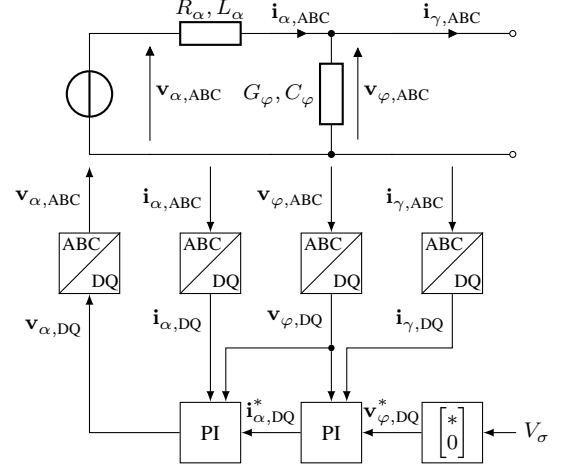


Fig. 4. Schematic diagram of a grid-forming CIDER with an LC filter.

Hypothesis 6. Irrespective of the type of CIDER, the reference angle θ , w.r.t. which the DQ frame is defined, is given by

$$\theta = 2\pi f_1 t + \theta_0 \quad (23)$$

where θ_0 is a known offset.

If this hypothesis holds, the Fourier coefficients of the transformation matrices (21)–(22), which are needed for the harmonic-domain model, are given as follows:

$$\mathbf{T}_{\pi|\kappa,+1} = \sqrt{\frac{2}{3}} \exp(j\theta_0) \begin{bmatrix} \frac{1}{2} & -\frac{1}{2j} \\ \frac{1}{2}\alpha^* & -\frac{1}{2j}\alpha^* \\ \frac{1}{2}\alpha & -\frac{1}{2j}\alpha \end{bmatrix} \quad (24)$$

$$\mathbf{T}_{\pi|\kappa,-1} = \mathbf{T}_{\pi|\kappa,+1}^* \quad (25)$$

where $\alpha = \exp(j\frac{2\pi}{3})$. As explained in Part I, the Fourier coefficients of time-periodic matrices appear on the diagonals of the associated Toeplitz matrices in the harmonic domain. For example, the coefficients of order $h = \pm 1$ appear on the first upper and lower diagonal, respectively. Accordingly, $\hat{\mathbf{T}}_{\kappa|\pi}$ and $\hat{\mathbf{T}}_{\pi|\kappa}$ have a block band structure, which introduces coupling between the harmonics.

Having specified the reference frames, the FF gain $\mathbf{K}_{\text{FF},\lambda}$ as given in Hyp. 5 can be evaluated. By substitution of (21)–(22) and Hyp. 6 into (13) and (16), one can show that

$$\mathbf{R}_{\lambda,\text{DQ}} = \begin{bmatrix} R_\lambda & -2\pi f_1 L_\lambda \\ 2\pi f_1 L_\lambda & R_\lambda \end{bmatrix} \quad (26)$$

$$\mathbf{G}_{\lambda,\text{DQ}} = \begin{bmatrix} G_\lambda & -2\pi f_1 C_\lambda \\ 2\pi f_1 C_\lambda & G_\lambda \end{bmatrix} \quad (27)$$

The off-diagonal elements are a.k.a. decoupling terms [5].

B. Grid-Forming Resource

Fig. 4 shows the schematic diagram of a typical grid-forming CIDER. Its power hardware consists of a PWM actuator and an LC filter, and its control software of a two-stage PI controller. The actuator is a four-leg power converter which can inject or absorb homopolar currents. This feature is of crucial importance for islanded operation, during which the grid-forming CIDER takes the role of the slack.

The state of the power hardware is given by the inductor current $\mathbf{i}_{\alpha,ABC} \in \mathbb{R}^{3 \times 1}$ and the capacitor voltage $\mathbf{v}_{\varphi,ABC} \in \mathbb{R}^{3 \times 1}$. The input and disturbance are the actuator voltage $\mathbf{v}_{\alpha,ABC} \in \mathbb{R}^{3 \times 1}$ and grid current $\mathbf{i}_{\gamma,ABC} \in \mathbb{R}^{3 \times 1}$, respectively. The output includes both state and disturbance. That is

$$\mathbf{x}_\pi(t) = \begin{bmatrix} \mathbf{i}_{\alpha,ABC}(t) \\ \mathbf{v}_{\varphi,ABC}(t) \end{bmatrix} \in \mathbb{R}^{6 \times 1} \quad (28)$$

$$\mathbf{u}_\pi(t) = \mathbf{v}_{\alpha,ABC}(t) \in \mathbb{R}^{3 \times 1} \quad (29)$$

$$\mathbf{w}_\pi(t) = \mathbf{i}_{\gamma,ABC}(t) \in \mathbb{R}^{3 \times 1} \quad (30)$$

$$\mathbf{y}_\pi(t) = \begin{bmatrix} \mathbf{x}_\pi(t) \\ \mathbf{w}_\pi(t) \end{bmatrix} \in \mathbb{R}^{9 \times 1} \quad (31)$$

The time-domain state-space model of the power hardware is obtained by combining the differential equations (2) and (3) of the filter stages. This yields

$$\mathbf{A}_\pi(t) = \begin{bmatrix} -\mathbf{L}_\alpha^{-1}\mathbf{R}_\alpha & -\mathbf{L}_\alpha^{-1} \\ \mathbf{C}_\varphi^{-1} & -\mathbf{C}_\varphi^{-1}\mathbf{G}_\varphi \end{bmatrix} \quad (32)$$

$$\mathbf{B}_\pi(t) = \begin{bmatrix} \mathbf{L}_\alpha^{-1} \\ \mathbf{0}_{3 \times 3} \end{bmatrix} \quad (33)$$

$$\mathbf{E}_\pi(t) = \begin{bmatrix} \mathbf{0}_{3 \times 3} \\ -\mathbf{C}_\varphi^{-1} \end{bmatrix} \quad (34)$$

$$\mathbf{C}_\pi(t) = \begin{bmatrix} \text{diag}(\mathbf{1}_6) \\ \mathbf{0}_{3 \times 6} \end{bmatrix} \quad (35)$$

$$\mathbf{D}_\pi(t) = \mathbf{0}_{9 \times 3} \quad (36)$$

$$\mathbf{F}_\pi(t) = \begin{bmatrix} \mathbf{0}_{6 \times 3} \\ \text{diag}(\mathbf{1}_3) \end{bmatrix} \quad (37)$$

The sizes of these matrices follow directly from (28)–(31). Note that these matrices are time-invariant, which means that only the Fourier coefficient for $h = 0$ is nonzero. For instance:

$$\mathbf{A}_\pi(t) = \mathbf{A}_{\pi,0} \quad (38)$$

The same holds for the other matrices of the state-space model. Accordingly, the power hardware is an LTI system, which is a particular case of an LTP system.

Recall from Hyp. 3 that each controller stage consists of one PI controller (i.e., for FB control) and two P controllers (i.e., for FF and FT control). Since the control software is composed of PI controllers, its state is given by the temporal integrals of the errors w.r.t. the inductor current $\Delta \mathbf{i}_{\alpha,DQ} \in \mathbb{R}^{2 \times 1}$ and the capacitor voltage $\Delta \mathbf{v}_{\varphi,DQ} \in \mathbb{R}^{2 \times 1}$. Its input and output are defined by the interconnection with the power hardware as shown in Fig. 4. The disturbance is the reference voltage $\mathbf{v}_{\varphi,DQ}^* \in \mathbb{R}^{2 \times 1}$ of the outer controller stage. Accordingly

$$\mathbf{x}_\kappa(t) = \int \begin{bmatrix} \Delta \mathbf{i}_{\alpha,DQ}(t) \\ \Delta \mathbf{v}_{\varphi,DQ}(t) \end{bmatrix} dt \in \mathbb{R}^{4 \times 1} \quad (39)$$

$$\mathbf{u}_\kappa(t) = \begin{bmatrix} \mathbf{i}_{\alpha,DQ}(t) \\ \mathbf{v}_{\varphi,DQ}(t) \\ \mathbf{i}_{\gamma,DQ}(t) \end{bmatrix} \in \mathbb{R}^{6 \times 1} \quad (40)$$

$$\mathbf{w}_\kappa(t) = \mathbf{v}_{\varphi,DQ}^*(t) \in \mathbb{R}^{2 \times 1} \quad (41)$$

$$\mathbf{y}_\kappa(t) = \mathbf{v}_{\alpha,DQ}(t) \in \mathbb{R}^{2 \times 1} \quad (42)$$

The time-domain state-space model of the control software is found by combining the differential equations (6) and (8) of the controller stages. This gives

$$\mathbf{A}_\kappa(t) = \begin{bmatrix} \mathbf{0}_{2 \times 2} & \frac{\mathbf{K}_{FB,\varphi}}{T_{FB,\varphi}} \\ \mathbf{0}_{2 \times 2} & \mathbf{0}_{2 \times 2} \end{bmatrix} \quad (43)$$

$$\mathbf{B}_\kappa(t) = \begin{bmatrix} -\text{diag}(\mathbf{1}_2) & -\mathbf{K}_{FB,\varphi} & \mathbf{K}_{FT,\varphi} \\ \mathbf{0}_{2 \times 2} & -\text{diag}(\mathbf{1}_2) & \mathbf{0}_{2 \times 2} \end{bmatrix} \quad (44)$$

$$\mathbf{E}_\kappa(t) = \begin{bmatrix} \mathbf{K}_{FF,\varphi} + \mathbf{K}_{FB,\varphi} \\ \text{diag}(\mathbf{1}_2) \end{bmatrix} \quad (45)$$

$$\mathbf{C}_\kappa(t) = \begin{bmatrix} \frac{\mathbf{K}_{FB,\alpha}}{T_{FB,\alpha}} & (\mathbf{K}_{FF,\alpha} + \mathbf{K}_{FB,\alpha}) \frac{\mathbf{K}_{FB,\varphi}}{T_{FB,\varphi}} \end{bmatrix} \quad (46)$$

$$\mathbf{D}_\kappa(t) = [-\mathbf{K}_{FB,\alpha} \quad (\mathbf{D}_\kappa)_2 \quad (\mathbf{D}_\kappa)_3] \quad (47)$$

$$(\mathbf{D}_\kappa)_2 = \mathbf{K}_{FT,\alpha} - (\mathbf{K}_{FF,\alpha} + \mathbf{K}_{FB,\alpha}) \mathbf{K}_{FB,\varphi} \quad (48)$$

$$(\mathbf{D}_\kappa)_3 = (\mathbf{K}_{FF,\alpha} + \mathbf{K}_{FB,\alpha}) \mathbf{K}_{FT,\varphi} \quad (49)$$

$$\mathbf{F}_\kappa(t) = (\mathbf{K}_{FF,\alpha} + \mathbf{K}_{FB,\alpha})(\mathbf{K}_{FF,\varphi} + \mathbf{K}_{FB,\varphi}) \quad (50)$$

The sizes of these matrices follow directly from (39)–(42). Evidently, the control software is an LTI system, too. Indeed, this is one of the reasons for the popularity of the DQ frame since its invention almost a century ago [6].

In grid-forming CIDERS, the reference angle θ is computed from the frequency setpoint f_σ through integration over time

$$\theta = 2\pi \int f_\sigma dt = 2\pi f_\sigma t \quad (51)$$

Hence, in line with Hyp. 6, the following hypothesis is made.

Hypothesis 7. *In steady state, the frequency setpoints of all grid-forming CIDERS are equal to the fundamental frequency:*

$$f_\sigma = f_1 \quad (52)$$

Indeed, if the grid-forming CIDERS attempted to impose incompatible frequencies on the power system, no steady-state equilibrium could exist. As discussed in Part I, the setpoints for the resource-level controllers are determined by system-level controllers. Since system-level controllers act on a substantially slower timescale than resource-level ones, the steady-state values of the setpoints can be determined in an independent analysis (i.e., prior to the HPF study).

The reference voltage $\mathbf{v}_{\varphi,DQ}^*$ is calculated from the voltage setpoint V_σ as follows:

Hypothesis 8. *The reference voltage for the grid-forming CIDERS is calculated as follows*

$$\mathbf{v}_{\varphi,DQ}^*(t) = \sqrt{\frac{3}{2}} \begin{bmatrix} V_\sigma \\ 0 \end{bmatrix} \quad (53)$$

where V_σ is the setpoint for the peak voltage.

C. Grid-Following Resource

Fig. 5 shows the schematic diagram of a typical grid-following CIDER. Its power hardware consists of a PWM actuator and an LCL filter, and its control software of a three-stage PI controller. The actuator is a three-leg power converter, which is commonly used for grid-following CIDERS.

The state of the power hardware is described by the inductor currents $\mathbf{i}_{\alpha,ABC} \in \mathbb{R}^{3 \times 1}$ and $\mathbf{i}_{\gamma,ABC} \in \mathbb{R}^{3 \times 1}$ and the capacitor

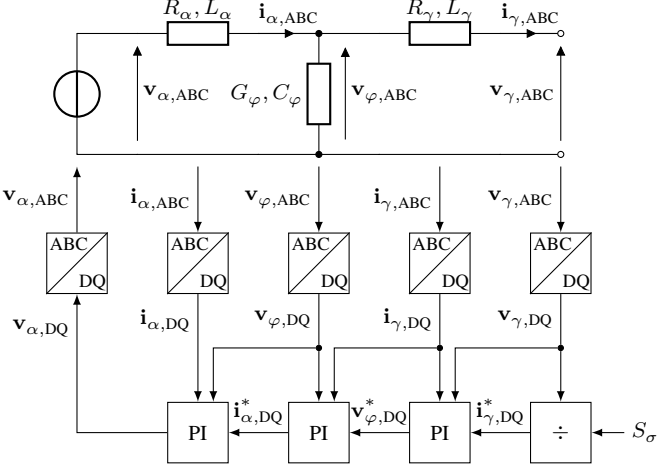


Fig. 5. Schematic diagram of a grid-following CIDER with an LCL filter.

voltage $\mathbf{v}_{\varphi,\text{ABC}} \in \mathbb{R}^{3 \times 1}$. The input is the actuator voltage $\mathbf{v}_{\alpha,\text{ABC}} \in \mathbb{R}^{3 \times 1}$ and the disturbance is the grid voltage $\mathbf{v}_{\gamma,\text{ABC}} \in \mathbb{R}^{3 \times 1}$. The output consists of the state and the disturbance. Formally

$$\mathbf{x}_\pi(t) = \begin{bmatrix} \mathbf{i}_{\alpha,\text{ABC}}(t) \\ \mathbf{v}_{\varphi,\text{ABC}}(t) \\ \mathbf{i}_{\gamma,\text{ABC}}(t) \end{bmatrix} \in \mathbb{R}^{9 \times 1} \quad (54)$$

$$\mathbf{u}_\pi(t) = \mathbf{v}_{\alpha,\text{ABC}}(t) \in \mathbb{R}^{3 \times 1} \quad (55)$$

$$\mathbf{w}_\pi(t) = \mathbf{v}_{\gamma,\text{ABC}}(t) \in \mathbb{R}^{3 \times 1} \quad (56)$$

$$\mathbf{y}_\pi(t) = \begin{bmatrix} \mathbf{x}_\pi(t) \\ \mathbf{w}_\pi(t) \end{bmatrix} \in \mathbb{R}^{12 \times 1} \quad (57)$$

The matrices of the state-space model are obtained as

$$\mathbf{A}_\pi(t) = \begin{bmatrix} -\mathbf{L}_\alpha^{-1}\mathbf{R}_\alpha & -\mathbf{L}_\alpha^{-1} & \mathbf{0}_{3 \times 3} \\ \mathbf{C}_\varphi^{-1} & -\mathbf{C}_\varphi^{-1}\mathbf{G}_\varphi & -\mathbf{C}_\varphi^{-1} \\ \mathbf{0}_{3 \times 3} & \mathbf{L}_\gamma^{-1} & -\mathbf{L}_\gamma^{-1}\mathbf{R}_\gamma \end{bmatrix} \quad (58)$$

$$\mathbf{B}_\pi(t) = \begin{bmatrix} \mathbf{L}_\alpha^{-1} \\ \mathbf{0}_{6 \times 3} \end{bmatrix} \quad (59)$$

$$\mathbf{E}_\pi(t) = \begin{bmatrix} \mathbf{0}_{6 \times 3} \\ -\mathbf{L}_\varphi \end{bmatrix} \quad (60)$$

$$\mathbf{C}_\pi(t) = \begin{bmatrix} \text{diag}(\mathbf{1}_9) \\ \mathbf{0}_{3 \times 9} \end{bmatrix} \quad (61)$$

$$\mathbf{D}_\pi(t) = \mathbf{0}_{12 \times 3} \quad (62)$$

$$\mathbf{F}_\pi(t) = \begin{bmatrix} \mathbf{0}_{9 \times 3} \\ \text{diag}(\mathbf{1}_3) \end{bmatrix} \quad (63)$$

Their sizes follow straightforward from (54)–(57). Note that these matrices are time-invariant as in the grid-forming case.

Analogously, the state-space variables of the control software are given by

$$\mathbf{x}_\kappa(t) = \int \begin{bmatrix} \Delta \mathbf{i}_{\alpha,\text{DQ}}(t) \\ \Delta \mathbf{v}_{\varphi,\text{DQ}}(t) \\ \Delta \mathbf{i}_{\gamma,\text{DQ}}(t) \end{bmatrix} dt \in \mathbb{R}^{6 \times 1} \quad (64)$$

$$\mathbf{u}_\kappa(t) = \begin{bmatrix} \mathbf{i}_{\alpha,\text{DQ}}(t) \\ \mathbf{v}_{\varphi,\text{DQ}}(t) \\ \mathbf{i}_{\gamma,\text{DQ}}(t) \\ \mathbf{v}_{\gamma,\text{DQ}}(t) \end{bmatrix} \in \mathbb{R}^{8 \times 1} \quad (65)$$

$$\mathbf{w}_\kappa(t) = \mathbf{i}_{\gamma,\text{DQ}}^*(t) \in \mathbb{R}^{2 \times 1} \quad (66)$$

$$\mathbf{y}_\kappa(t) = \mathbf{v}_{\alpha,\text{DQ}}(t) \in \mathbb{R}^{2 \times 1} \quad (67)$$

The matrices of the state-space model are obtained as

$$\mathbf{A}_\kappa(t) = \begin{bmatrix} \mathbf{0}_{2 \times 2} & \frac{\mathbf{K}_{\text{FB},\varphi}}{T_{\text{FB},\varphi}} (\mathbf{K}_{\text{FB},\varphi} + \mathbf{K}_{\text{FF},\varphi}) \frac{\mathbf{K}_{\text{FB},\gamma}}{T_{\text{FB},\gamma}} \\ \mathbf{0}_{2 \times 2} & \mathbf{0}_{2 \times 2} \\ \mathbf{0}_{2 \times 2} & \mathbf{0}_{2 \times 2} \end{bmatrix} \quad (68)$$

$$\mathbf{B}_\kappa(t) = \begin{bmatrix} (\mathbf{B}_\kappa)_{11} & -\mathbf{K}_{\text{FB},\varphi} & (\mathbf{B}_\kappa)_{13} & (\mathbf{B}_\kappa)_{14} \\ \mathbf{0}_{2 \times 2} & (\mathbf{B}_\kappa)_{22} & -\mathbf{K}_{\text{FB},\gamma} & \mathbf{K}_{\text{FT},\gamma} \\ \mathbf{0}_{2 \times 2} & \mathbf{0}_{2 \times 2} & (\mathbf{B}_\kappa)_{33} & \mathbf{0}_{2 \times 2} \end{bmatrix} \quad (69)$$

$$(\mathbf{B}_\kappa)_{ii} = -\text{diag}(\mathbf{1}_2) \quad \forall i \quad (70)$$

$$(\mathbf{B}_\kappa)_{13} = \mathbf{K}_{\text{FT},\varphi} - (\mathbf{K}_{\text{FB},\varphi} + \mathbf{K}_{\text{FF},\varphi})\mathbf{K}_{\text{FB},\gamma} \quad (71)$$

$$(\mathbf{B}_\kappa)_{14} = (\mathbf{K}_{\text{FB},\varphi} + \mathbf{K}_{\text{FF},\varphi})\mathbf{K}_{\text{FT},\gamma} \quad (72)$$

$$\mathbf{E}_\kappa(t) = \begin{bmatrix} (\mathbf{K}_{\text{FB},\varphi} + \mathbf{K}_{\text{FF},\varphi})(\mathbf{K}_{\text{FB},\gamma} + \mathbf{K}_{\text{FF},\gamma}) \\ \mathbf{K}_{\text{FB},\gamma} + \mathbf{K}_{\text{FF},\gamma} \\ \text{diag}(\mathbf{1}_2) \end{bmatrix} \quad (73)$$

$$\mathbf{C}_\kappa(t) = \begin{bmatrix} \frac{\mathbf{K}_{\text{FB},\alpha}}{T_{\text{FB},\alpha}} & (\mathbf{K}_{\text{FB},\alpha} + \mathbf{K}_{\text{FF},\alpha}) \frac{\mathbf{K}_{\text{FB},\varphi}}{T_{\text{FB},\varphi}} & (\mathbf{C}_\kappa)_3 \end{bmatrix} \quad (74)$$

$$(\mathbf{C}_\kappa)_3 = (\mathbf{K}_{\text{FB},\alpha} + \mathbf{K}_{\text{FF},\alpha})(\mathbf{K}_{\text{FB},\varphi} + \mathbf{K}_{\text{FF},\varphi}) \frac{\mathbf{K}_{\text{FB},\gamma}}{T_{\text{FB},\gamma}} \quad (75)$$

$$\mathbf{D}_\kappa(t) = [-\mathbf{K}_{\text{FB},\alpha} \quad (\mathbf{D}_\kappa)_2 \quad (\mathbf{D}_\kappa)_3 \quad (\mathbf{D}_\kappa)_4] \quad (76)$$

$$(\mathbf{D}_\kappa)_2 = \mathbf{K}_{\text{FT},\alpha} - (\mathbf{K}_{\text{FB},\alpha} + \mathbf{K}_{\text{FF},\alpha})\mathbf{K}_{\text{FB},\varphi} \quad (77)$$

$$(\mathbf{D}_\kappa)_3 = (\mathbf{K}_{\text{FB},\alpha} + \mathbf{K}_{\text{FF},\alpha}) \begin{pmatrix} \mathbf{K}_{\text{FT},\varphi} \\ -(\mathbf{K}_{\text{FB},\varphi} + \mathbf{K}_{\text{FF},\varphi})\mathbf{K}_{\text{FB},\gamma} \end{pmatrix} \quad (78)$$

$$(\mathbf{D}_\kappa)_4 = (\mathbf{K}_{\text{FB},\alpha} + \mathbf{K}_{\text{FF},\alpha})(\mathbf{K}_{\text{FB},\varphi} + \mathbf{K}_{\text{FF},\varphi})\mathbf{K}_{\text{FB},\gamma} \quad (79)$$

$$\mathbf{F}_\kappa(t) = \prod_{\lambda \in \{\alpha, \varphi, \gamma\}} \{\mathbf{K}_{\text{FB},\lambda} + \mathbf{K}_{\text{FF},\lambda}\} \quad (80)$$

Their sizes follow straightforward from (64)–(67). Note that these matrices are also time-invariant.

In grid-following CIDERs, the reference angle θ needed for the DQ transform is provided by a synchronization unit, usually a *Phase-Locked Loop* (PLL). The reference current $\mathbf{i}_{\gamma,\text{DQ}}^*$ is computed in order to track the power setpoint $S_\sigma = P_\sigma + jQ_\sigma$ at the fundamental frequency. Without imposing any further conditions on θ , $\mathbf{i}_{\gamma,\text{DQ}}^*$ is given by

$$\mathbf{i}_{\gamma,\text{DQ}}^*(t) = \frac{1}{v_{\gamma,\text{D}}^2(t) + v_{\gamma,\text{Q}}^2(t)} \begin{bmatrix} v_{\gamma,\text{D}}(t) & -v_{\gamma,\text{Q}}(t) \\ v_{\gamma,\text{Q}}(t) & v_{\gamma,\text{D}}(t) \end{bmatrix} \begin{bmatrix} P_\sigma \\ Q_\sigma \end{bmatrix} \quad (81)$$

In the vast majority of cases, synchronization units in general and PLLs in particular are designed to lock to the fundamental positive-sequence component of the grid voltage (e.g., [7]). This working principle leads to the following hypothesis:

Hypothesis 9. *The synchronization units of the grid-following CIDERs lock to the fundamental positive-sequence component of the grid voltage. Therefore, in steady state it holds that*

$$V_{\gamma,\text{Q},0} = \frac{1}{T} \int v_{\gamma,\text{Q}}(t) dt = 0 \quad (82)$$

For instance, this can be achieved by a closed-loop controller which adjusts θ in order to regulate $v_{\gamma,\text{Q}}$ to 0 on average.

As required by power quality standards (e.g., [1]), the grid voltages have to be maintained balanced and sinusoidal within specified limits³. Under these conditions, it follows that

Hypothesis 10. *The time-variant signal content of $v_{\gamma,D}(t)$ and $v_{\gamma,Q}(t)$, as given by $\xi_D(t)$ and $\xi_Q(t)$ below, is low:*

$$v_{\gamma,D}(t) = V_{\gamma,D,0}(1 + \xi_D(t)), |\xi_D(t)| \ll 1 \quad (83)$$

$$v_{\gamma,Q}(t) = V_{\gamma,Q,0}(1 + \xi_Q(t)), |\xi_Q(t)| \ll 1 \quad (84)$$

As a consequence of Hyps. 9 and 10, $v_{\gamma,Q}(t)$ can be neglected w.r.t. $v_{\gamma,D}(t)$ in (81):

$$\mathbf{i}_{\gamma,DQ}^*(t) = \frac{1}{v_{\gamma,D}(t)} \begin{bmatrix} P_\sigma \\ Q_\sigma \end{bmatrix} \quad (85)$$

In order to calculate the harmonic-domain closed-loop transfer function of the CIDER, the Fourier coefficients of $\mathbf{i}_{\gamma,DQ}^*$ are needed. Unfortunately, the exact expressions which relate the Fourier coefficients of the reciprocal $v_{\gamma,D}^{-1}$ and those of $v_{\gamma,D}$ are complicated [8], and their evaluation is computationally intensive. However, taking advantage of Hyp. 10, the following approximation is made:

Hypothesis 11. *For the calculation of the reference current in the grid-following CIDERs, the reciprocal of the grid voltage is approximated by a second-order Taylor series*

$$\frac{1}{v_{\gamma,D}(t)} \approx \frac{1}{V_{\gamma,D,0}} \left(1 - \xi_D(t) + \xi_D^2(t) \right) \quad (86)$$

Let Ψ_h be the Fourier coefficients of the Taylor approximation of the reciprocal $v_{\gamma,D}^{-1}(t)$:

$$\frac{1}{v_{\gamma,D}(t)} \approx \sum_h \Psi_h \exp(jh2\pi f_1 t) \quad (87)$$

These Fourier coefficients are obtained by substituting

$$\xi_D(t) = \sum_{h \neq 0} \frac{V_{\gamma,D,h}}{V_{\gamma,D,0}} \exp(jh2\pi f_1 t) \quad (88)$$

into the Taylor series, and expanding the second-order term. This yields

$$\Psi_h = \begin{cases} \frac{1}{V_{\gamma,D,0}} + \sum_{h \neq 0} \frac{|V_{\gamma,D,h}|^2}{V_{\gamma,D,0}^3} & h = 0 \\ -\frac{V_{\gamma,D,h}}{V_{\gamma,D,0}^2} + \sum_{i \neq 0} \frac{V_{\gamma,D,i} V_{\gamma,D,h-i}}{V_{\gamma,D,0}^3} & \text{otherwise} \end{cases} \quad (89)$$

Note well that, since the Taylor series in Hyp. 11 is of second order, the approximation of the PQ control law (85) is a nonlinear function of the Fourier coefficients.

D. Accordance with the Proposed Generic Model

The previously discussed models are perfectly in accordance with the generic model presented in Part I of this paper, provided that the listed hypotheses hold. Therefore, the suitability of the generic model to represent different types of CIDERs can be confirmed at this point.

³By contrast, the grid currents may be subject to unbalances and harmonics.

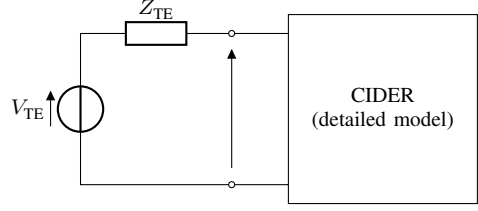


Fig. 6. Test setup for the validation of the HPF method on individual CIDERs. The resource is represented by a detailed state-space model (see Section III), and the power system by a Thévenin equivalent (see Tables I and II).

TABLE I
SHORT-CIRCUIT PARAMETERS OF THE THÉVENIN EQUIVALENT

Parameter	Resource Validation	System Validation	Description
V_n	230 V-RMS	230 V-RMS	Nominal voltage
S_{sc}	267 kW	3.85 MW	Short-circuit power
$ Z_{sc} $	195 mΩ	13.7 mΩ	Short-circuit impedance
R_{sc}/X_{sc}	6.207	0.271	Resistance-to-reactance ratio

IV. VALIDATION OF THE PROPOSED METHOD ON INDIVIDUAL RESOURCES

A. Methodology and Key Performance Indicators

For the validation of the proposed modelling framework for CIDERs, the test setup shown in Fig. 6 is used. It consists of two parts: a *Thévenin Equivalent* (TE) that represents the grid, and a detailed model of the CIDER under investigation. The TE impedance is characterized by typical short-circuit parameters of a power distribution grid, which are given in Table I. The TE voltage source includes harmonics, whose levels are given in Table II. These levels are set according to the limits specified in the standard BS-EN-50160:2000 [1]. In line with this standard, harmonics up to order 25 (i.e., 1.25 kHz) are considered in the HPF study. Note that, a TE voltage source with the maximum permissible distortion at each harmonic frequency corresponds to a stressed grid. This condition is deemed most suitable for the validation of the HPF method, because it poses a challenge to the modelling framework. Moreover, it is crucial that the results are reliable when the system is under stress.

The exemplary parameters for the grid-forming and grid-following CIDER are listed in Tables III and IV, respectively. The filter parameters were derived following the design rules proposed in [9]. The setpoints are $V_\sigma = 241.5$ V-RMS and $f_\sigma = 50$ Hz for the grid-forming CIDER, and $P_\sigma = 50$ kW and $Q_\sigma = 16.4$ kVAr for the grid-following one.

The HPF models and method discussed in Part I of this paper were implemented in Matlab, and compared against *Time-Domain Simulations* (TDS) with averaged models of the CIDERs in Simulink (recall Hyp. 1). The TDS are stopped once steady-state is reached, and the spectra are calculated using the *Discrete Fourier Transform* (DFT) on a time window composed by the last 5 periods of the fundamental frequency of the obtained signals. All analyses are performed in normalized units w.r.t. the base power $P_b = 10$ kW and the base voltage $V_b = 230$ V-RMS.

TABLE II

HARMONIC VOLTAGES OF THE THÉVENIN EQUIVALENT (SEE [1]).

h	$ V_{TE,h} $	$\angle V_{TE,h}$
1	1.0 p.u.	0.00 deg
5	6.0 %	22.50 deg
7	5.0 %	15.00 deg
11	3.5 %	11.25 deg
13	3.0 %	22.50 deg
17	2.0%	15.00 deg
19	1.5 %	11.25 deg
23	1.5 %	11.25 deg

TABLE III

PARAMETERS OF THE GRID-FORMING RESOURCE
(RATED POWER 100 kVA)

Filter stage	L/C	R/G	K_{FB}	T_{FB}	K_{FT}
Inductor (α)	0.2 mH	0.61 mΩ	15	0.03	1
Capacitor (φ)	150 μF	0 S	0.05	2.5E-4	0

In order to assess the accuracy and performance of the proposed method, suitable *Key Performance Indicators* (KPIs) have to be defined. The accuracy is quantified by the errors of the harmonic phasors obtained using the HPF method w.r.t. the DFT spectra of the time-domain signals. Let \mathbf{X}_h denote the Fourier coefficient of a polyphase electrical quantity (i.e., voltage or current). The KPIs are defined as follows:

$$e_{\text{abs}}(\mathbf{X}_h) := \max_p ||X_{h,p,\text{HPF}}| - |X_{h,p,\text{TDS}}|| \quad (90)$$

$$e_{\arg}(\mathbf{X}_h) := \max_p |\angle X_{h,p,\text{HPF}} - \angle X_{h,p,\text{TDS}}| \quad (91)$$

So, $e_{\text{abs}}(\mathbf{X}_h)$ and $e_{\arg}(\mathbf{X}_h)$ are the maximum absolute errors in magnitude and phase, respectively, over all phases $p \in \mathcal{P}$.

B. Results and Discussion

The result for the grid-forming and grid-following CIDER are shown in Figs. 7a and 7b, respectively. For the sake of simplicity, only the controlled quantities are shown: that is, the output voltage of the grid-forming CIDER, and the output current of the grid-following CIDER. The spectra on the left-hand sides of Figs. 7a and 7b show that the Fourier coefficients obtained using HPF and TDS are congruent both in magnitude and phase. This is confirmed by the error plots on the right-hand sides of the figures. The maximum errors are $e_{\text{abs}}(\mathbf{V}_5) = 3.01\text{E-}5$ p.u. and $e_{\arg}(\mathbf{V}_5) = 0.06$ deg for the grid-forming resource, and $e_{\text{abs}}(\mathbf{I}_7) = 4.95\text{E-}4$ p.u. and $e_{\arg}(\mathbf{I}_{25}) = 0.46$ deg for the grid-following one. These values are below the accuracy of standard measurement equipment (i.e., they are negligible in practice).

TABLE IV

PARAMETERS OF THE GRID-FOLLOWING RESOURCE
(RATED POWER 60 kVA)

Filter stage	L/C	R/G	K_{FB}	T_{FB}	K_{FT}
Actuator-side inductor (α)	325 μH	1.02 mΩ	10.5	6.6e-4	1
Capacitor (φ)	90.3 μF	0 S	1	2.6e-3	0
Grid-side inductor (γ)	325 μH	1.02 mΩ	0.2	0.1	1

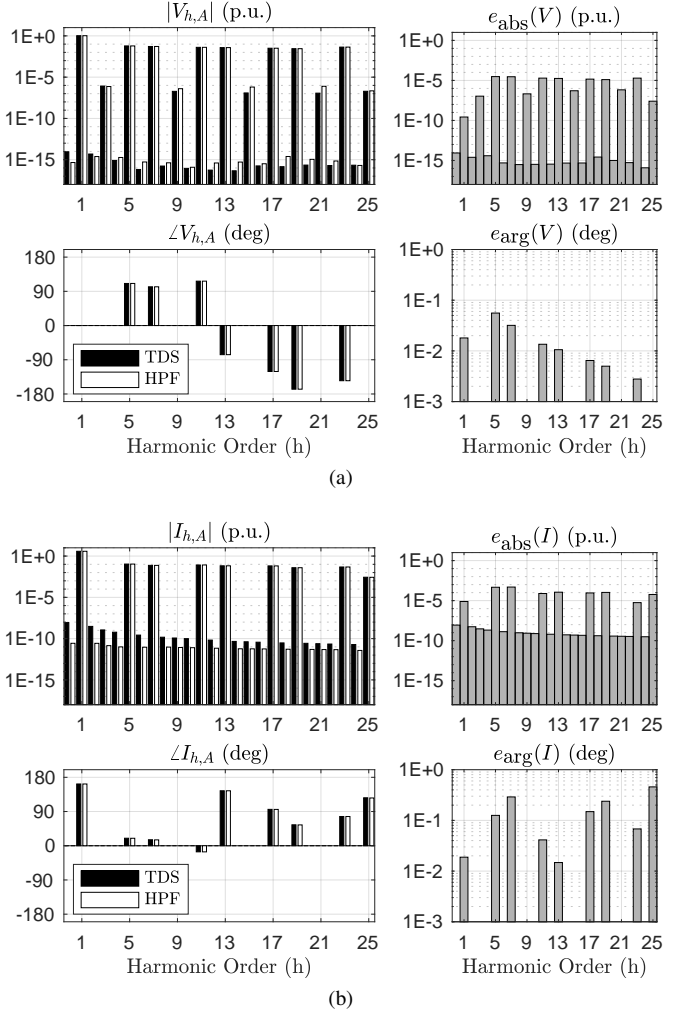


Fig. 7. Results of the validation on individual grid-forming (7a) and grid-following (7b) CIDERs. The plots on the left-hand side show the spectra (i.e., for phase A), and the ones on the right-hand side the error.

V. VALIDATION OF THE PROPOSED METHOD ON AN ENTIRE SYSTEM

A. Methodology and Key Performance Indicators

Lastly, the proposed HPF method is applied to the test system shown in Fig. 8, which is adapted from the CIGRÉ low-voltage benchmark microgrid [10]. That is, the HPF problem is formulated for the complete system model, and solved numerically using the Newton-Raphson method (see Section V in Part I).

The test system is characterized as follows. The substation is located in node N1. Its short-circuit parameters, which include both the substation transformer and the upstream grid, are listed in Table I. The lines are built from underground

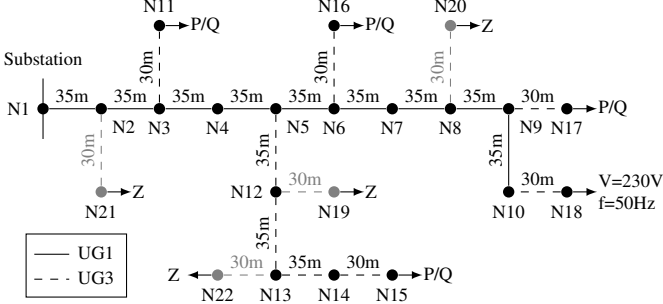


Fig. 8. Schematic diagram of the test system, which is based on the CIGRÉ low-voltage benchmark microgrid [10] (in black) and extended by unbalanced impedance loads (in grey). For the cable parameters see Table V. The set of grid-following resources are composed of constant impedance loads (Z) and constant power loads (P/Q), their parameters are given in Table VI.

TABLE V
SEQUENCE PARAMETERS OF THE LINES IN THE TEST SYSTEM.

ID	R_+/R_-	R_0	L_+/L_-	L_0	C_+/C_-	C_0
UG1	0.162 Ω	0.529 Ω	0.262 mH	1.185 mH	637 nF	388 nF
UG3	0.822 Ω	1.794 Ω	0.270 mH	3.895 mH	637 nF	388 nF

cables, whose sequence parameters are given in Table V. Note that, while the proposed HPF method can treat frequency-dependent cable parameters (see Section III in Part I), the parameters of the benchmark microgrid are considered to be frequency-independent. A preliminary analysis was conducted with EMTP-RV in order to confirm that this approximation does hold well on the frequency range under consideration (i.e., ≤ 1.25 kHz). For further details, please see Appendix A. Five CIDERs are connected to the ends of the side feeders (i.e., in nodes N11 and N15-18): one grid-forming and four grid-following ones. Their parameters are the same as for the resource validation, see Tables III and IV. Additionally, unbalanced wye-connected constant-impedance loads, are connected at nodes N19-22. The unbalance of a load is expressed by phase weights, which indicate the distribution of the load among the phases. The setpoints and parameters of the grid-following resources are given in Table VI, the setpoints of the grid-forming resources in Fig. 8. Notably, the load unbalance is set such that the resulting voltage unbalance does not exceed the limits specified in [1] (i.e., $|V_{1,-}| \leq 2\% \cdot |V_{1,+}|$).

As stated in Part I of this paper, the HPF problem is a system of nonlinear equations, which are solved numerically by means of the Newton-Raphson method. Due to its nonlinearity, the HPF problem may have multiple solutions, one or several of which may not even be physically meaningful. As known from numerical analysis, the convergence of an iterative numerical solver to a particular solution can be affected by the choice of the initial point. Therefore, it is crucial to verify whether multiplicity of solutions occurs, and whether the convergence is robust w.r.t. the initial point. In order to assess the convergence behaviour of the proposed HPF method, the initial spectra of voltages and currents are varied. More precisely, the initial spectra are obtained as a superposition of random positive, negative, and homopolar sequences at each frequency

TABLE VI
PARAMETERS OF THE GRID-FOLLOWING RESOURCES AND LOADS IN THE TEST SYSTEM.

Node	S	pf	Type	Phase weights
N11	15.0 kW	0.95	P/Q	[0.33 0.33 0.33]
N15	52.0 kW	0.95	P/Q	[0.33 0.33 0.33]
N16	55.0 kW	0.95	P/Q	[0.33 0.33 0.33]
N17	35.0 kW	0.95	P/Q	[0.33 0.33 0.33]
N19	51.2 kW	0.95	Z	[0.31 0.50 0.19]
N20	51.7 kW	0.95	Z	[0.45 0.23 0.32]
N21	61.5 kW	0.95	Z	[0.24 0.39 0.37]
N22	61.9 kW	0.95	Z	[0.31 0.56 0.13]

(i.e., fundamental and harmonics), whose magnitudes and phases are uniformly distributed in the intervals $[0, 10]$ p.u. and $[0, 2\pi]$ rad, respectively.

The accuracy of the HPF method is assessed by means of the same KPIs used for the individual resources: the magnitude and phase errors of the HPF results w.r.t. DFT spectra of time-domain waveforms. A detailed performance analysis of the HPF study is conducted. To this end, the method's performance is quantified by the mean and standard deviation of the execution time of the HPF study through $N = 50$ simulations and compared to the execution time of the TDS (incl. the Fourier analysis). Moreover, a scalability analysis w.r.t. the numbers of CIDERs and w.r.t. the considered harmonic order in the HPF is performed. In the first case, the grid-following CIDERs at nodes N15-17 are consecutively replaced by wye-connected, balanced impedance loads, whose nominal power is equal to the setpoint of the associated CIDER. In the second case, the timing analysis for the HPF is repeated while increasing the considered maximum harmonic order h_{max} consecutively from 11 to 25. It is important to note that the TDS takes some time to reach the steady state. The settling time of this transient analysis strongly depends on the initialization of the simulation. In order to ensure a fair comparison between the HPF and the TDS, the execution time of the latter is measured only for 5 periods in steady state (i.e., the window length required for the DFT) plus the Fourier analysis (i.e., the DFT). Note well that this corresponds to the minimum amount of simulation time which would have to be done even if the initialization of the TDS were perfect.

B. Results and Discussion

Table VII gives the voltage and current sequence components of the nodes where resources are connected. Indeed the passive impedance loads at N19-22 introduce significant unbalances in the nodal phase-to-ground voltages and injected currents.

The convergence of the method appears to be robust w.r.t. a random choice of the initial point (i.e., sequence components whose magnitudes and phases are uniformly distributed in the intervals $[0, 10]$ p.u. and $[0, 2\pi]$ rad, respectively). In fact, the method always converged to the same solution irrespective of its initial value. That is, neither divergence of the algorithm nor multiplicity of solutions have been observed. Naturally, this empirical evidence does not provide a general guarantee.

TABLE VII
RATIO OF SEQUENCE VOLTAGES AND CURRENTS
AT THE NODES WITH RESOURCES

Node	$\frac{ V_{1,-} }{ V_{1,+} }$	$\frac{ V_{1,0} }{ V_{1,+} }$	$\frac{ I_{1,-} }{ I_{1,+} }$	$\frac{ I_{1,0} }{ I_{1,+} }$
N1	0.26 %	0.19 %	12.78 %	9.04 %
N11	0.46 %	0.77 %	0.24 %	0.00 %
N15	1.63 %	3.76 %	0.32 %	0.00 %
N16	0.53 %	0.80 %	0.11 %	0.00 %
N17	0.48 %	0.51 %	0.13 %	0.00 %
N18	0.47 %	0.23 %	0.14 %	3.92 %
N19	1.38 %	3.17 %	26.19 %	24.45 %
N20	0.40 %	0.77 %	19.67 %	18.90 %
N21	0.48 %	0.61 %	13.18 %	13.38 %
N22	1.95 %	4.57 %	37.09 %	34.36 %

Nevertheless, the fact that the convergence is not affected even by substantial variations of the initial point speaks for the robustness of the proposed method.

Fig. 9 shows the maximum absolute errors over all nodes and phases, separately for grid-forming and grid-following CIDERs. The highest errors w.r.t. voltage magnitude and phase are $e_{\text{abs}}(V_{19}) = 6.33E-5$ p.u. and $e_{\text{arg}}(V_{23}) = 0.37$ deg, respectively. The highest errors w.r.t. current magnitude and phase are $e_{\text{abs}}(I_1) = 1.33E-3$ p.u. and $e_{\text{arg}}(I_{25}) = 0.87$ deg, respectively. Observe that the magnitude errors of the current harmonics are higher than those of the voltage harmonics, which is likely due to the Taylor approximation in the reference calculation of the grid-following CIDERs (i.e., Hyp. 11). Moreover, note that the phase error becomes slightly larger as the harmonic order increases. Nevertheless, the error levels are generally very low. Indeed, as it was the case in the resource validation, the magnitude and phase errors are lower than the accuracy of standard measurement equipment.

All simulations are run on the same laptop computer, namely a MacBook Pro 2019 with a 2.4 GHz Intel Core i9 CPU and 32 GB 2400 MHz DDR3 RAM. As shown in Table VIII, the mean of the execution time of the HPF method lies between 1.75-6.52 sec with standard deviations from 0.03-0.1 sec depending on the number of CIDERs that are connected. By comparison, the execution time of the TDS is around 28.33-33.39 sec, out of which ca. 0.6 sec are needed for the Fourier analysis (i.e., the DFT). Clearly, the HPF method is faster than the TDS, while yielding accurate results. The computational complexity of the HPF method in function of the maximum harmonic order is illustrated in the upper subplot of Fig. 10. Note that the execution time increases almost linearly, but a non-dominant higher-order component is clearly visible (i.e., as expected based on the involved matrix operations). The non-deterministic component of $T_{\text{exc,HPF}}$ (i.e., the variation around the mean value) is illustrated in the lower subplot of Fig. 10. Observe that any deviation is small compared to the actual value of $T_{\text{exc,HPF}}$.

VI. CONCLUSIONS

In Part II of this paper, the HPF method proposed in Part I was validated. It was confirmed that common types of CIDERs (i.e., power converters with LC and LCL filters) can well be represented using the proposed modelling framework.

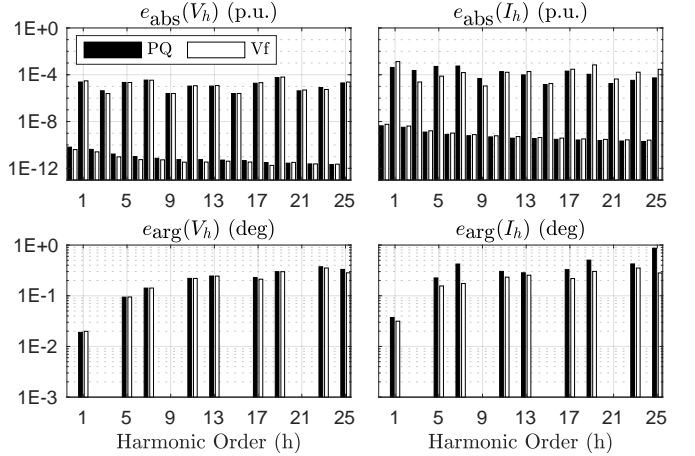


Fig. 9. Results of the validation on the benchmark system. The plots show the maximum absolute errors over all nodes and phases, for voltages (left column) and currents (right column), in magnitude (top row) and phase (bottom row).

TABLE VIII
TIMING PERFORMANCE (FOR $N = 50$ SIMULATIONS OF THE HPF)

No. of Following CIDERs	1	2	3	4
$T_{\text{exc,TDS}}$	28.33 sec	30.36 sec	31.28 sec	33.39 sec
$\mu(T_{\text{exc,HPF}})$	1.75 sec	3.97 sec	5.30 sec	6.52 sec
$\sigma(T_{\text{exc,HPF}})$	0.03 sec	0.07 sec	0.08 sec	0.10 sec

Moreover, the HPF method was implemented in Matlab and validated against time-domain simulations with Simulink. For this validation, both individual resources as well as an entire system (i.e., the CIGRÉ low-voltage benchmark microgrid) were investigated. The largest observed errors are 1.33E-3 p.u. w.r.t. current magnitude, 6.33E-5 p.u. w.r.t. voltage magnitude, and 0.87 deg w.r.t. phase. If run on a standard laptop computer, the execution of the HPF method for the benchmark system is up to five times faster as compared to the TDS (incl. the Fourier analysis). These results confirm that the proposed approach is indeed accurate and computationally efficient.

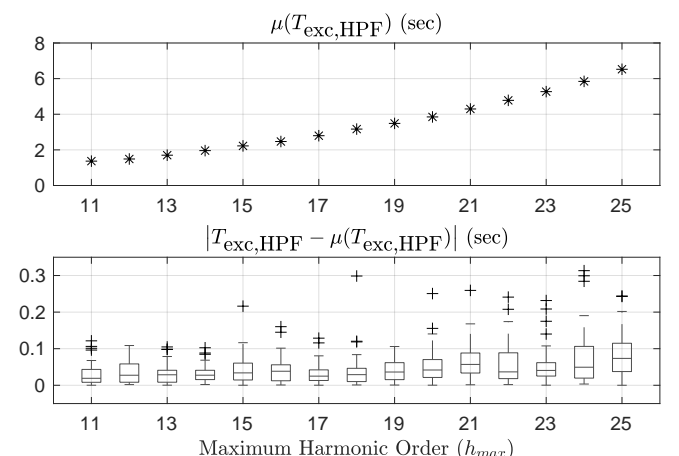


Fig. 10. Mean and distribution of the timing performance of HPF for maximum numbers of CIDERs and with varying h_{max} for $N = 50$ simulations. The box-and-whisker plot visualizes 25 and 75 percentile of the sample, the whisker length is 1.5-times the interquartile range.

APPENDIX A

FREQUENCY-DEPENDENT CABLE PARAMETERS

A. Impact on the Branch Admittance of the Line Model

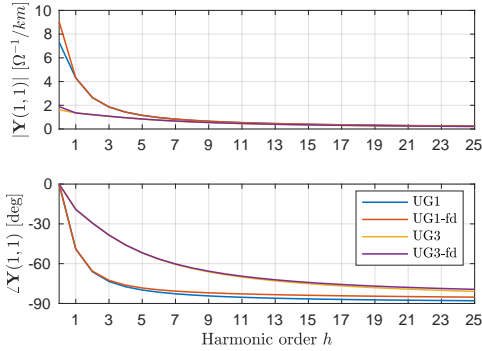


Fig. 11. Comparison of line branch admittances of the π -section equivalents with/without frequency-dependence of the cable parameters. For illustration, the element $(1, 1)$ of the compound admittance matrices of the cable types (i.e., UG1 and UG3) is shown. The curves labelled with the suffix “fd” correspond to the cable models with frequency-dependent parameters.

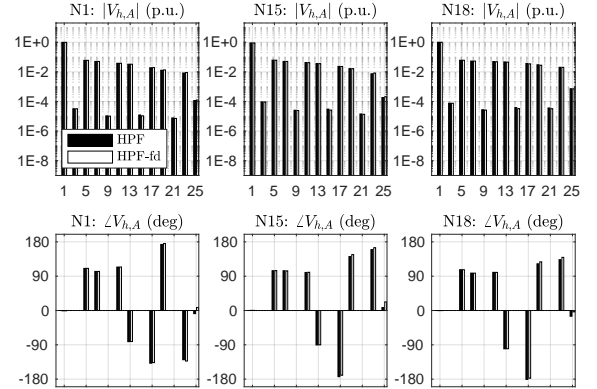
The CIGRÉ report [10], in which the benchmark microgrid is specified, does not provide any information on the frequency dependency of the cable parameters. Therefore, the cable parameters were calculated using EMTP-RV based on the available data on cable material and geometry. The behaviour of the branch admittances as function of frequency is shown in Figure 11. For illustration, the element $(1, 1)$ of the compound admittance matrices are shown. As one can see, whether or not the frequency dependency of the parameters is considered has virtually no impact on the magnitude of the line admittance. In the phase, there is a slight difference between the two models at higher frequencies.

B. Impact on the Results of the Harmonic Power-Flow Study

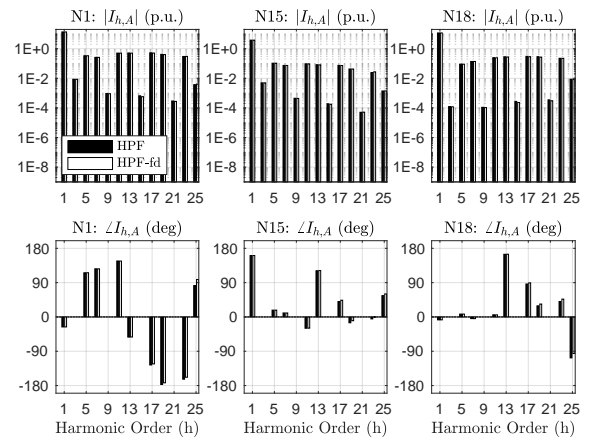
In order to assess the impact on the results of the HPF study, analyses were conducted on the benchmark system using either the line model with frequency-invariant or -dependent parameters. The obtained results are shown in Figure 12. For illustration, the comparison is done at three nodes throughout the benchmark system. The results are compared at three nodes throughout the system. As one can see, the spectra obtained using the different line models are congruent. This is in line with the previously discussed analyses made in EMTP-RV.

REFERENCES

- [1] “Voltage characteristics of electricity supplied by public distribution networks,” British Standards Institution, London, UK, Std. BS-EN-50160:2000, 2000.
- [2] F. Blaabjerg, Z. Chen, and S. B. Kjaer, “Power electronics as efficient interface in dispersed power generation systems,” *IEEE Trans. Power Electron.*, vol. 19, no. 5, pp. 1184–1194, 2004.
- [3] F. Blaabjerg *et al.*, “Overview of control and grid synchronization for distributed power generation systems,” *IEEE Trans. Ind. Electron.*, vol. 53, no. 5, pp. 1398–1409, 2006.
- [4] J. Wang *et al.*, “Design of a generalized control algorithm for parallel inverters for smooth microgrid transition operation,” *IEEE Trans. Ind. Electron.*, vol. 62, no. 8, pp. 4900–4914, 2015.
- [5] J. Rocabert *et al.*, “Control of power converters in AC microgrids,” *IEEE Trans. Power Electron.*, vol. 27, no. 11, pp. 4734–4749, 11 2012.



(a)



(b)

Fig. 12. Impact of the frequency-dependent parameters on the results of the HPF study. The results are compared at three nodes throughout the benchmark system. The currents for Phase A are given in (12b) and the voltages in (12a). The results labelled with the suffix “fd” correspond to the line models with frequency-dependent parameters.

- [6] R. H. Park, “Two-reaction theory of synchronous machines,” *Trans. AIEE*, vol. 48, no. 3, pp. 716–727, 7 1929.
- [7] R. Teodorescu *et al.*, *Grid Converters for Photovoltaic and Wind Power Systems*. John Wiley & Sons, 2011, vol. 29.
- [8] A. Edrei and G. Szegő, “A note on the reciprocal of a Fourier series,” *Proc. AMS*, vol. 4, no. 2, pp. 323–329, 1953.
- [9] M. Liserre, F. Blaabjerg, and S. Hansen, “Design and control of an LCL-filter-based three-phase active rectifier,” *IEEE Trans. Ind. Appl.*, vol. 41, no. 5, pp. 1281–1291, 2005.
- [10] K. Strunz *et al.*, “Benchmark systems for network integration of renewable and distributed energy resources,” CIGRÉ, Paris, IDF, FR, Tech. Rep. 575, 2014.



Johanna Kristin Maria Becker (S’19) received the B.Sc. degree in Microsystems Engineering from Freiburg University, Germany in 2015 and the M.Sc. degree in Electrical Engineering from the Swiss Federal Institute of Technology of Lausanne (EPFL), Lausanne, Switzerland in 2019. She is currently pursuing a Ph.D. degree at the Distributed Electrical System Laboratory, EPFL, with a focus on robust control and stability assessment of active distribution systems in presence of harmonics.



Andreas Martin Kettner (S'15-M'19) received the M.Sc. degree in electrical engineering and information technology from the Swiss Federal Institute of Technology of Zürich (ETHZ), Zürich, Switzerland in 2014, and the Ph.D. degree in power systems engineering from the Swiss Federal Institute of Technology of Lausanne (EPFL), Lausanne, Switzerland in 2019. He was a postdoctoral researcher at the Distributed Electrical Systems Laboratory (DESL) of EPFL from 2019 to 2020. Since then, he has been working as a project engineer for PSI NEPLAN AG in Küsnacht, Switzerland and continues to collaborate with DESL.



Lorenzo Reyes-Chamorro (S'13-M'16-SM'20) was born in Santiago, Chile in 1984. He received the B.Sc. degree in electrical engineering from the University of Chile, Santiago, Chile in 2009 and the Ph.D. degree at the Swiss Federal Institute of Technology of Lausanne (EPFL), Lausanne, Switzerland in 2016. He was a postdoctoral fellow at the Distributed Electrical System Laboratory, EPFL from 2016 to 2018. He is currently Assistant Professor in the Institute of Electricity and Electronics and Director of the Innovative Energy Technologies Center (INVENT UACH) at Universidad Austral de Chile, Valdivia, Chile.



Zhixiang Zou (S'12-M'18-SM'20) received the B.Eng. and Ph.D. degrees in electrical and engineering from Southeast University, Nanjing, China, in 2007 and 2014, respectively, the Dr.-Ing. degree (summa cum laude) from Kiel University, Germany, in 2019. He was an engineer in the State Grid Electric Power Research Institute, Nanjing, China, from 2007 to 2009. He was a research fellow at the Chair of Power Electronics, Kiel University, Germany, from 2014 to 2019. He is now an associate professor in the School of Electrical Engineering at the Southeast University. His research interests include smart transformers, microgrid stability, modeling and control of power converters. Dr. Zou serves as an Associate Editor of the IEEE Open Journal of Power Electronics, an Associate Editor of the IEEE Access, an Editor of the International Transactions on Electrical Energy Systems, and an Editor of the Mathematical Problem in Engineering, and a Standing Director of IEEE PES Power System Relaying & Control Satellite Committee.



Marco Liserre (S'00-M'02-SM'07-F'13) received the MSc and PhD degree in Electrical Engineering from the Bari Polytechnic, respectively in 1998 and 2002. He has been Associate Professor at Bari Polytechnic and from 2012 Professor in reliable power electronics at Aalborg University (Denmark). From 2013 he is Full Professor and he holds the Chair of Power Electronics at Kiel University (Germany). He has published 500 technical papers (1/3 of them in international peer-reviewed journals) and a book. These works have received more than 35000 citations. Marco Liserre is listed in ISI Thomson report “The world’s most influential scientific minds” from 2014. He has been awarded with an ERC Consolidator Grant for the project “The Highly Efficient And Reliable smart Transformer (HEART), a new Heart for the Electric Distribution System”. He is member of IAS, PELS, PES and IES. He has been serving all these societies in different capacities. He has received the IES 2009 Early Career Award, the IES 2011 Anthony J. Hornfeck Service Award, the 2014 Dr. Bimal Bose Energy Systems Award, the 2011 Industrial Electronics Magazine best paper award in 2011 and 2020 and the Third Prize paper award by the Industrial Power Converter Committee at ECCE 2012, 2012, 2017 IEEE PELS Sustainable Energy Systems Technical Achievement Award and the 2018 IEEE-IES Mittelmann Achievement Award.



Mario Paolone (M'07-SM'10) received the M.Sc. (Hons.) and Ph.D. degrees in electrical engineering from the University of Bologna, Italy, in 1998 and 2002. In 2005, he was an Assistant Professor in power systems with the University of Bologna, where he was with the Power Systems Laboratory until 2011. Since 2011, he has been with the Swiss Federal Institute of Technology, Lausanne, Switzerland, where he is Full Professor and the Chair of the Distributed Electrical Systems Laboratory. His research interests focus on power systems with reference to real-time protections, dynamics and transients. Dr. Paolone has authored or co-authored over 300 papers published in mainstream journals and international conferences in the area of energy and power systems that received numerous awards including the IEEE EMC Technical Achievement Award, two IEEE Transactions on EMC best paper awards, the IEEE Power System Dynamic Performance Committee's prize paper award and the Basil Papadis best paper award at the 2013 IEEE PowerTech. Dr. Paolone was the founder Editor-in-Chief of the Elsevier journal Sustainable Energy, Grids and Networks.